Hemesh Avireddy*, Joan Ramon Morante and Cristina Flox

A Perspective: Could Carbon Current Collectors Improve the Energy Density of Aqueous Alkaline Symmetric Supercapacitors?

DOI 10.1515/ehs-2016-0015

Abstract: The present discussion shows a perspective about using graphite as a current collector in order to achieve high energy density in a symmetric supercapacitor system. Several electrochemical modes (such as rest potential analysis, CV, PEIS, GCPL) were carried out to evaluate the electrochemical characteristics of graphite in aqueous 6 mol/L KOH. And, the resulting performance was compared to an another conventional current collector system based on nickel-stainless steel. Interestingly, widening of cell voltage was observed for graphite when compared to nickel-stainless steel. The discussion reveals the reasonable influences and validations of widening in cell voltage towards the values in energy densities. This perspective also highlights some issues related to carbon (graphite) current collectors and encloses with some promising strategies in overcoming these issues, not limiting the domain of application (either micro or macro supercapacitor devices).

Keywords: current collectors, cell voltage, energy density, Fe_2O_3 porous carbon nanofibers, single spinneret electrospinning

1 Introduction

One of the major goals set by the European Union was to withdraw at least 20 % of its energy consumption from the renewable resources such as wind or solar energy by the year 2020. The important criterion of these renewable resources is the equipped energy storage device. Electrochemical storage devices such as supercapacitors (SCs) could deliver requisite energy in a short interval of time. In this regard, many groups around the world focus their research in developing high performance SCs. However, SCs suffers from low energy density when compared to batteries (Béguin et al. 2014; Simon et al. 2014). In SCs, energy density is expressed as $0.5*CE^2$ where, C represents the cell capacitance (F) and E as the cell voltage (V). To enhance the energy density of a SC, two strategies could be implemented: increasing cell capacitance and voltage (Béguin et al. 2014; Dai et al. 2015).

In the first aspect, the capacitance could be enriched by tuning the electrochemical active materials independance with their type of charge storage phenomena, which could be classified into: (a) electrostatic sorption of ions in the material´s pores (ultra-micropores <~0.7 nm or micropores <2 nm; electric double layer capacitance, EDLC) and (b) highly reversible multiple redox reactions occurring over the electrode potential window (pseudocapacitance) or reversible redox reactions favorable at high rates (Brousse et al. 2015; Salanne et al. 2016). Extensive research has been focused on developing hybrid systems besides improving existing promising carbon materials and transition metal oxides (examples: Carbon-CNTs, Graphene, Carbide derived Carbons and porous Carbons nanofibers; Transition metal oxides- RuO_2, MnO_2, Co_3O_4 and Fe_2O_3) (Béguin et al. 2014; Dai et al. 2015; Gao et al. 2015; Lukatskaya et al. 2016; Zhang et al. 2015).

In regards to the second aspect, cell voltage could be enhanced by using electrolytes with wider thermodynamic potential windows such as organic (~2.5 V) and ionic liquids (~>3.5 V). However, these electrolytes could be disadvantageous because of their low ionic conductivities, high costs and nature of less environmental friendliness. Aqueous electrolytes could be an another substitute due to their nature of high ionic conductivities, cost effectiveness and environmental friendliness (Béguin et al. 2014; Demarconnay et al. 2010). However, aqueous electrolytes provides low cell voltages (~1.0 V) due to the low thermodynamic potential window of water (1.23 V),

***Corresponding author: Hemesh Avireddy,** IREC, Catalonia Institute for Energy Research. Jardins de les Dones de Negre 1, 08930. Sant Adrià de Besòs, Spain; Departament d'Electronica, Universitat de Barcelona, 08028 Barcelona, Spain, E-mail: ahemesh@irec.cat
http://orcid.org/0000-0002-0679-859X
Joan Ramon Morante, IREC, Catalonia Institute for Energy Research. Jardins de les Dones de Negre 1, 08930. Sant Adrià de Besòs, Spain; Departament d'Electronica, Universitat de Barcelona, 08028 Barcelona, Spain
Cristina Flox, IREC, Catalonia Institute for Energy Research. Jardins de les Dones de Negre 1, 08930. Sant Adrià de Besòs, Spain

eventually leading to low energy densities (Abbas et al. 2015; Béguin et al. 2014; Demarconnay et al. 2010).

Interestingly, François Béguin´s group was able to show an excellent cyclable 1.9 V carbon/carbon symmetric SC using 1 mol/L Li_2SO_4 (Abbas et al. 2015; Fic et al. 2012; Q. Gao et al. 2012). The high cell voltage was achieved because of the optimization in high over potential of di-hydrogen evolution, contributed from water reduction and OH^- ions produced from negative carbon pores (Abbas et al. 2015; Demarconnay et al. 2010; Gao et al. 2012). However, this system was designed with a cell composed of gold current collectors which could reduce the feasibility of commercialization. In order to reduce the high cost involved due to the usage of gold, stainless steel was implemented and a cell voltage of 1.5 V was achieved (Abbas et al. 2015). Beyond 1.5 V, for example at 1.6 V, reduction of capacitance was observed due to increase in cell resistance which was likely due to the accumulation and generations of corrosion products. These products could be contributed due to the irreversible oxygen evolving reactions at the positive end (Abbas et al. 2015; Ratajczak et al. 2013; Ratajczak et al. 2014). Furthermore, since thanks to the nickel´s ability to avoid corrosion at the positive end as compared with stainless steel, stainless steel was replaced by nickel. Although mixed nickel compounds are formed due to oxidation of $Ni(OH)_2$ to NiOOH, apparently not much influence has been observed on the electrochemical performances. This effect might be due to the good conductivity of mixed nickel compounds, which could provide high mobility to electronic and ionic species (Abbas et al. 2015). While, on close observations on these discussions, the limiting factor of cell voltage could be from current collectors. In this regard, as carbon/carbon system with gold current collectors could show 1.9 V, we percept about using carbon itself as a current collector which is currently the motivation of this work.

Therefore, in the present discussion, we show a perspective about using carbon as current collector in a symmetric prototype cell configuration. Graphite was chosen primitively to validate this perspective in a traditional aqueous alkaline medium (6 mol/L KOH). The agenda of varying the electrolyte from 1 mol/L Li_2SO_4 to 6 mol/L KOH was due to the high solubility of KOH in water when compared with that of Li_2SO_4 (KOH = 121 g/100 ml; Li_2SO_4, monohydrate = 34.9 g/100 ml at 25 °C), which could provide high ionic conductivity and mobility to electrolyte ions (Béguin et al. 2014). In addition, we also compare this perspective with nickel-stainless steel current collectors. In addition to this, flexibile self standing Fe_2O_3 porous carbon nanofibers (Fe_2O_3-PCNFs) were prepared via single spinneret electrospinning technique under a high feed rate. These electrode materials are promising active materials for both micro and macro-supercapacitors because of the presence in two-fold charge storage effects (EDLC (Zhang et al. 2015) and redox reactions (Li et al. 2015)).

2 Methods and Materials

2.1 Chemicals

Polyacrylonitrile (99 %, PAN; M_w: 150 000) and Ferric chloride, (99 %, $FeCl_3$) were purchased from Sigma Aldrich. Whereas N, N-dimethylformamide (99 %, DMF) as a solvent from Panreac and Potassium hydroxide (KOH, M_w: 56.11; pellets) from Emsure. All chemicals were used without further purification.

2.2 Fabrication of Electrode Materials

The mixture of 3 wt. % of $FeCl_3$ and 12 wt. % of PAN was dissolved in 20 g of DMF solution by magnetic stirring for an hour at 80 °C to obtain a homogenous electrospinning blend solution. The weight percent (wt. %) in case of PAN would represent the weight with respect to the weight content of DMF solvent, whereas, in case of $FeCl_3$, weight content of Fe in $FeCl_3$ with respect to PAN. The blend solutions were electrospun on an electrospinning rotating type current collector system obtained from Yflow® Nanotechology Solutions (Flox et al. 2013) (as shown in Figure 1), with optimized electrospinning parameters to fabricate a mat. The applied voltage, feed rate and distance between the spinneret and current collector was around 14 kV (1.75 kV/cm^2), 1.50 mL/h and 8 cm, respectively. The mats were stabilized in the air at 270 °C (7 h; 1 °C/min) and carbonized in Ar/H_2 (5 %) at 500 °C and 800 °C (1 h at each step; 5 °C/min) to obtain self-supporting flexible Fe_2O_3-PCNFs films (see Figure 1). These Fe_2O_3-PCNFs films were subjected to different material and electrochemical characterization techniques.

2.3 Material Characterization

Field Emission Scanning Electron Microscopy (FESEM) images and Energy-Dispersive X-ray Spectroscopy (EDS)

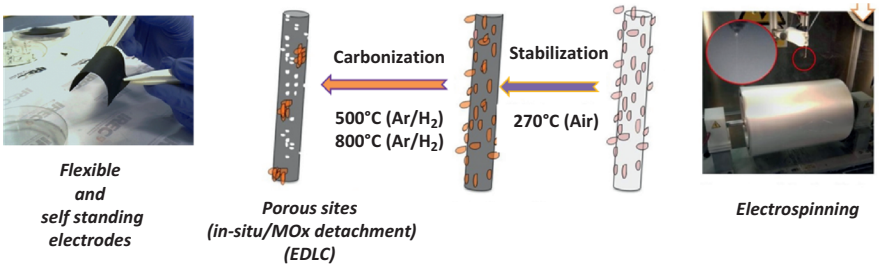

Figure 1: Right: An ongoing single spinneret electrospining process, Feed rate: 1.5 mL/h (Stage: production of mats). Left: Flexible and self-standing Fe_2O_3-PCNFs electrodes prepared via single spinneret electrospining technique. (Equipment: Yflow ® Nanotechnology solutions) (Flox et al. 2013).

were obtained by Zeiss Serie Auriga. Powered X-ray diffraction (P-XRD) analysis was observed using Bruker D8 advance equipment with CuKα1 radiation (λ=1.5405 Å). Transmission Electron Microscopy (TEM) images were obtained by Zeiss LIBRA 120 at different operating voltages (mainly from 50 kV to 75 kV). Thermogravimetric analysis (TGA) was obtained by using PerkinElmer (TGA 4000) analyzer in the air with a ramp rate of 10 °C/min. Textural behavior was analyzed from N_2 sorption isotherms with Micromeritics ASAP 2020 porosimeter at −196 °C. Brunauer–Emmett–Teller (BET) Surface Area Analysis was used to estimate surface area, whereas Barrett-Joyner-Halenda (BJH) method for Pore Size & Volume analysis. Samples were degassed at 200 °C in N_2 for 12 h before the analysis.

2.4 Electrochemical Characterization

In order to know the individual electrochemical performance of the fabricated Fe_2O_3-CNFs films, a three electrode test cell configuration was used which was obtained from Bio-Logic (France). Saturated Calomel Electrode (SCE) and platinum mesh was used as a reference and the counter electrode. The working electrode in this case, was fabricated by laminated Fe_2O_3-PCNFs on nickel foam and stainless mesh to ensure good contacts. The average mass loading of active materials (including CNFs) was about 1.65 mg/cm^2.

Two different cells were used: (i) PTFE Swagelok cell named C-I and (ii) home-made zero-gap (filter press) prototype cell, named C-II. In the Swagelok cell, nanoporous membranes were sandwiched by two stainless steel pistons (grade 304) with cross-sectional geometrical area of 1.13 cm^2. Fe_2O_3-PCNFs films were laminated on nickel foam (purity>99 %) using press-die equipment (5 MPa, 10 s) to form a working electrode. The home-made prototype cell, as shown in Figure 2(a)), was

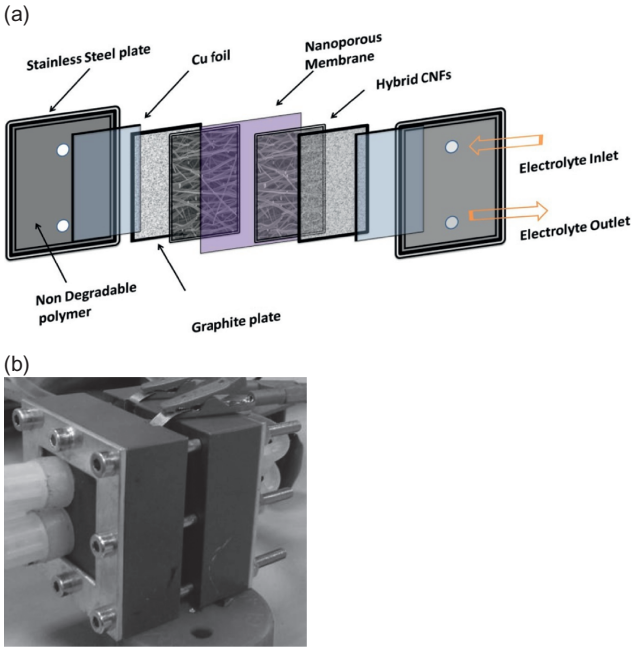

Figure 2: (a) Schematic representation of the prototype cell configuration with graphite as current collectors.

constructed by squeezing a nanoporous membrane with two graphite bipolar plates etched with serpentine flow channels. Each end of graphite plate was connected via cupper to make an electrical contact with cables of Potentiostat. Viton gaskets were used to avoid leakage of the electrolyte and metallic end-plates made up of aluminum were used to enclose the cell to ensure a zero-gap cell. (as shown in Figure 2(b)). The cell was injected with electrolyte through the inlets connected via tygon tubing. The electrochemical measurement was done in static mode. The geometrical area of the graphite to Fe_2O_3-PCNFs films was about 4 cm^2. In both cell configurations, equal mass loading of electrodes was used at both ends. The average mass loading of single electrode

was about 2.6 mg/cm^2 and 2.9 mg/cm^2 for C-I and C-II respectively.

The electrochemical characterization techniques such potentiostatic impedance spectroscopy (PEIS), cyclic Voltammetry (CV) and galvanostatic charge discharge cycles were performed by using a multichannel VMP3 potentiostat/galvanostat (Bio-Logic, France). PEIS was measured at a rest potential with amplitude of 5 mV/s from 200 kHz to 10 mHz. Long term stability experiments were measured in galvanostatic charge & discharge cycle mode using a cell current density of 1 A/g (>5000 cycles). The gravimetric capacitances (F/g) (for single electrode and cell) and energy density (Wh/kg) were calculated by considering the system as a non-linear SCs (see reference for methods (Laheäär et al. 2015).

3 Results and Discussions

3.1 Characterization of Fe_2O_3-PCNFs

The P-XRD pattern (as shown by Figure 3(a)) shows a broad peak in the 2 theta ranges of 20° to 30° and a narrow peak at 50, inferring the presence of amorphous carbon with graphitic impurities assigned to carbon (JCPDS card number of 01-075-1621). The remaining P-XRD peaks match the tetragonal structure of the maghemite phase of iron oxide (γ-Fe_2O_3; JCPDS card number: 25–1402). Moreover, the P-XRD pattern also shows a presence of low intensity peaks corresponding to the rhombohedral structure of hematite (α-Fe_2O_3; JCPDS card number: 33–0664) which might be due to the presence of a reducing atmosphere (Ar/H_2) or reducing effect of CNFs (Wu et al. 2014). The FESEM and TEM image, as shown in Figure 3(b) and 3(c), represents the morphological characteristics of continuously oriented CNFs incorporated into Fe_2O_3 nanostructures (nano-ball like morphology). In addition, an EDS element mapping was also evaluated, as shown in figure S4 (a)-(d), providing evidence of C, Fe and O distribution in the nanocomposite, which also indicates the Fe_2O_3 incorporation onto the surface of CNFs matrix. The thickness of the Fe_2O_3-CNFs film was around 210 µm (see supplementary, figure S1). Moreover, visible pores were also observed, providing a configuration of Fe_2O_3-PCNFs. These textural properties were further analyzed by N_2 adsorption measurements and their corresponding isotherms. BJH Pore Size & Volume distribution was represented by Figure 4(a) and 4(b) respectively. The isotherm shows a type I(b) and type IV(a) behavior with H2(a) or/and H2(b) type hysteresis,

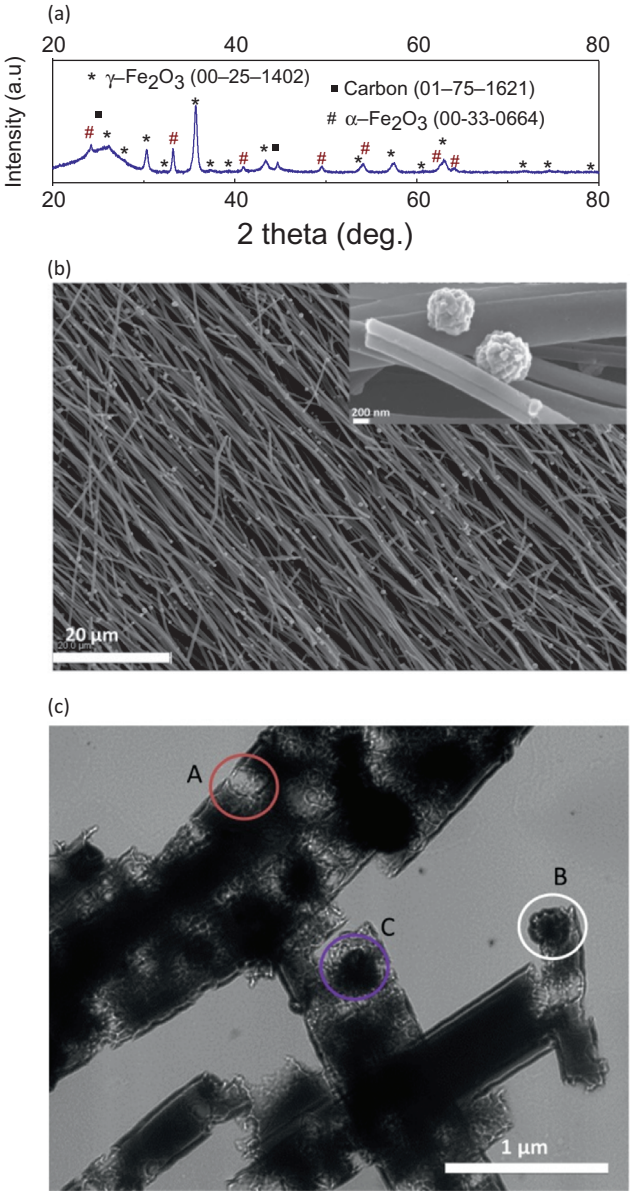

Figure 3: (a) P-XRD pattern of Fe_2O_3-PCNFs, (b) FESEM images of Fe_2O_3-PCNF (Inset image: Fe_2O_3 nanoballs like structures incorporated on CNF matrix, scale-200 nm) (c) TEM image of Fe_2O_3-PCNF (visible pores). A (Red): pores due to detachment of Fe_2O_3; B (white) and C (Purple): Fe_2O_3 nanoballs.

inferring broad range microporous (<~ 2.5 nm) and cylindrical mesoporous, which might be influenced by pore percolation caused by cavitation-induced evaporation (Thommes et al. 2015). In our case, the mesoporous was created by evaporation or etching of Fe_2O_3 during carbonization in Ar/H_2 (Ryu et al. 2013)). These pores exhibited microporosity between 1.79 nm to 2.0 nm, whereas mesoporosity occurred between 2.0 nm to 10.58 nm and 10.58 nm to 53.1 nm. The presence of a wide range of

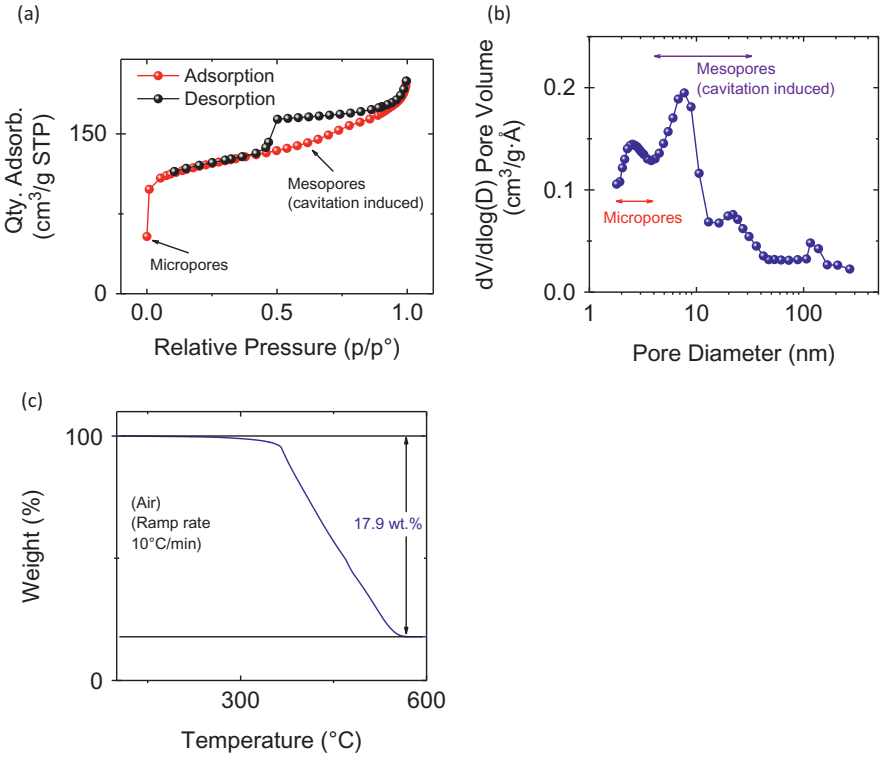

Figure 4: Textural analysis of Fe_2O_3-PCNFs (a) Nitrogen sorption curves, (b) corresponding adsorption pore size & volume distribution. (c) TGA curves, temperature for Initial measurement of weight %: 100 °C (X-axis).

porosity could provide better adsorption of electrolyte ions (EDLC) (Zhang et al. 2015). TGA measurement was conducted to calculate the wt. % of Fe_2O_3 incorporation on the CNFs matrix and is shown in Figure 4(c). Based on the results, the wt. % of Fe_2O_3 in CNF matrix was found to be around 17.9 wt. %.

3.2 Electrochemical Characterization

3.2.1 Cyclic Voltammetry

CV was conducted in order to: (i) understand the behavior of charge over the cell voltage window and (ii) identify the maximum cell operational voltage window. Figure 5 shows the CV curves for both C-I and C-II at a scan rate of 20 mV/s using Fe_2O_3-PCNFs as active materials (represented as gravimetric capacitance versus cell voltage, see supplementary figure S2 for current versus cell voltage). C-I exhibits almost rectangular shape behavior, where gravimetric capacitance is almost constant over the cell voltage window (Brousse et al. 2015). This behavior is typically related to the adsorption and desorption of electrolyte ions at the porous CNFs matrix,

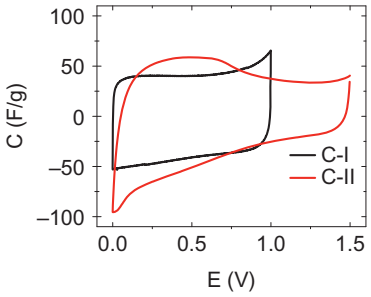

Figure 5: Cyclic voltammograms of Fe_2O_3-PCNFs in C-I (nickel-stainless steel) and C-II (graphite). (Two electrode cell configuration, scan rate: 20 mV/s and electrolyte: 6 mol/L KOH).

formed due to the decomposition of Fe_2O_3 during carbonization under Ar/H_2 atmosphere (Ryu et al. 2013). On the other hand, C-II exhibits an additional hump shape in the CV curve which might have been caused from augmented charge storage. These charge storage processes can be divided into two main regions, as shown in Figure 6: region 1 and 2. In region 1, charge contribution might have been the result of electrostatic adsorption of electrolyte ions at pores (similar to C-I). However, in region 2 (additional region), charge storage could have been

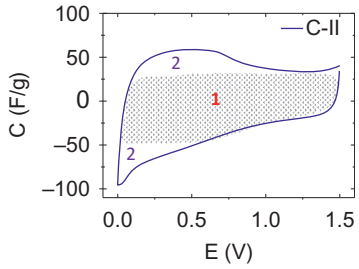

Figure 6: Cyclic voltammogram of Fe_2O_3-PCNFs in C-II (graphite). Region 1: electrostatic sorption of electrolyte ions. Region 2: redox reactions from Fe^0/ Fe^{2+}/Fe^{3+} and di-hydrogen formation and chemisorptions. (Two electrode cell configuration, scan rate: 20 mV/s and electrolyte: 6 mol/L KOH).

caused by di-hydrogen formation and chemisorptions, as well as by Fe_2O_3 assisted redox reactions. Further validation of this hypothesis was carried out by organizing CV in a three electrode cell experiment, as shown in Figure 7. To understand the charge storage processes, a potential window experiment was scheduled. In this experiment, working electrodes potential could be varied versus a standard reference electrode, eventually providing a behavior of current which could assist in distinguishing charge storage contributions. In this aspect, in our case, we vary the electrode potential window from 0.0 V to –1.2 V Vs. SCE (as shown in Figure 7). By contrast, three noticeable processes could be seen which were labeled as A, B and C, where A corresponds to electrostatic adsorption of electrolyte ions (EDLC), B corresponds to di-hydrogen production and chemisorptions which could be expressed by equations from [1] to [4], respectively.

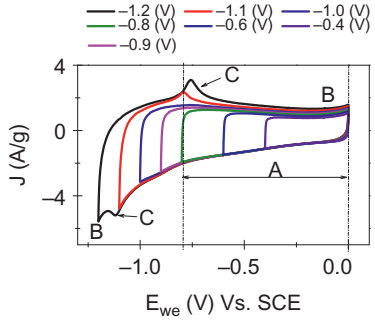

Figure 7: Three electrode cyclic voltammograms of Fe_2O_3-PCNFs with different potential windows. Label A: electrostatic sorption of electrolyte ions (EDLC). Label B: di-hydrogen formation and chemisorptions and label C: redox reactions from Fe^0/ Fe^{2+}/Fe^{3+}. (scan rate: 10 mV/s, electrolyte: 6 mol/L KOH, current collector: nickel-stainlees steel).

$$H_2O + e^- \rightarrow H + OH^- \quad (1)$$

$$\{C\} + xH \rightarrow \{CHx\} \quad (2)$$

$$C + xH_2O + xe^- \rightarrow \{CHx\} + OH^- \quad (3)$$

$$\{CHx\} + H_2O \rightarrow C + H_3O^+ + xe^- \quad (4)$$

In the above equations, {CHx} and {C} represent the hydrogen insertion into the carbon and carbon substrate, respectively (Abbas et al. 2015; Béguin et al. 2014). The charge storage from di-hydrogen production and chemisorptions has been previously observed with an increase in cell voltage for carbon/carbon SC (Abbas et al. 2015). These reactions could have been possibly originated from negative and/or the positive electrode during the negative potential scan (Demarconnay et al. 2010). On the other hand, label C corresponds to redox reactions attributed to $Fe^0/Fe^{2+}/Fe^{3+}$ in alkaline medium (Li et al. 2015). As a result, in case of C-II, because of these additional charge storage processes, an increase of capacitance (a hump) could be observed (when compared to C-I), achieving a single electrode gravimetric capacitance of about 63.1 F/g for C-II (whereas only 42.6 F/g could be reached with C-I) at a sweep rate of 20 mV/s. These capacitance values were appreciable when compared with those reported for Fe_2O_3 based 1 D and 2-D carbon electrodes in alkaline medium (as shown in Table. S1).

Interestingly (from Figure 5), CV provides information of maximum operating cell voltage, which was 1.0 V and 1.5 V for C-I and C-II, respectively. A lower cell voltage of 1.0 V was observed in case of C-I, compared with 1.5 V of C-II. The reason behind the limitation of cell voltage could be attributed to the irreversible oxygen evolving reactions from nickel-stainless steel current collector of positive side (Abbas et al. 2015). Moreover, no such observations were noticed until 1.5 V in case of C-II (see supplementary, as shown by figure S3). However, validation of these voltages as the maximum operating cell voltage is quite crucial and this has been carried out by voltage efficiency test.

3.2.2 Maximum Operating Cell Voltage (Supported by Voltage-Efficiency Test)

Voltage – efficiency test provides information about the maximum operating cell voltage (See references for meth-

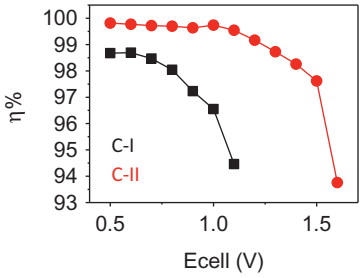

Figure 8: Plot between voltage-efficiency (observed by conducting galvanostatic charge & discharge cycles at a cell current density of 1 A/g).

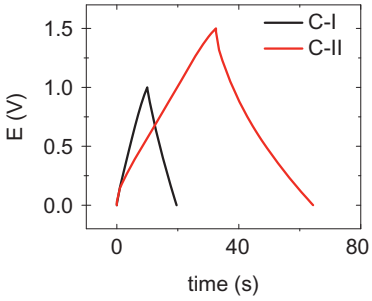

Figure 9: Galvanostatic charge & discharge cycle curves at a cell current density of 1 A/g. C-I (nickel-stainless steel) and C-II (graphite). (Electrolyte: 6 mol/L KOH. Two electrode cell configuration).

ods) (Abbas et al. 2015; Stoller and Ruoff n.d.). Conceptually, cell voltage is varied during this measurement, and the corresponding coulombic efficiency is usually observed. The cell voltage at which a drastic decrease in coulombic efficiency is noticed, we consider this voltage as the maximum operating cell voltage. In this point of view, we have varied cell voltage from 0.5 V to 1.1 V (for C-I) and 1.6 V (for C-II). Figure 8, shows the plot between coulombic efficiency (η%, $time_{discharge}$/$time_{charge}$) versus cell voltage. In case of C-I, the drastic change in η% was observed from 96.5 % to 94.4 %, when cell voltage was varied from 1.0 V to 1.1 V, whereas in case of C-II a coulombic efficiency of 97.6 % to 93.7 % was observed, when cell voltage was varied from 1.5 V to 1.6 V. As a result, the maximum operational cell voltage was concluded to be 1.0 V and 1.5 V for C-I and C-II, respectively, which correlates with our observations inferred during CV measurements (as shown in Figure 5). The wider cell voltage achieved in C-II could definitely influence the energy density, as energy density can be either improved by enhancing the cell capacitance or increasing the voltage (or both, relationship, Energy density = $0.5*CE^2$ (Béguin et al. 2014)).

3.2.3 Energy Density

The energy density was calculated from charge & discharge curves, which is shown in Figure 9 (current density: 1 A/g). With regards to the calculation of energy density, a difference in linear and non-linear SC system was considered. In a linear SC system, the charge (i. e. capacitance) is constant over the cell voltage window, whereas it is variable in a non-linear system. Since the variation of capacitance over the cell voltage for C-II was variable (due to additional charge storage processes, as discussed before), for comparison purposes, only a non-linear system is considered for both C-I and C-II. The gravimetric cell energy density and capacitances were calculated by the methods proposed by Laheäär et al. (2015). Lack of analysis about these points, i.e, misjudging the appropriate calculation methods for linear or non-linear systems could lead to an overestimation of energy density. An example has been shown in Table 1. The calculated energy density was about 1.21 Wh/kg and 5.05 Wh/kg for both C-I and C-II, respectively. From these values of energy density, the derived gravimetric cell capacitance was 8.73 F/g and 16.16 F/g for C-I and C-II, respectively. The observed energy density of C-II was almost increased by a factor of four. This increase in energy density could be accounted for because of: (1) the increase of cell voltage from 1.0 V to 1.5 V and (2) the additional charge storage contributions of di-hydrogen production and chemisorptions and redox reactions of $Fe^0/Fe^{2+}/Fe^{3+}$, which enhances the capacitance. These performance values indicate that the substitution of graphite (or carbon) instead of nickel-stainless steel current collectors could improve the energy density of SCs. However, validity at these cell voltages for long term performance is quite crucial.

Table 1: Values of electrochemical performances in terms of linear and non-linear SC system. C-I (nickel-stainless steel) and C-II (graphite).

Parameter	Linear System C-I	Linear System C-II	Non-linear System C-I	Non-linear System C-II
Gravimetric capacitance, Cell (F/g)	9.80	23.41	8.73	16.16
Energy density (Wh/kg)	1.36	7.31	1.21	5.05

3.2.4 Long Term Performance Studies (Charge & Discharge Cycles)

Long term performance stability in terms of capacitance retention for both C-I and C-II were analyzed by measuring 5,000 galvanostatic charge & discharge cycles at a cell current density of 1 A/g. The maximum cell voltage, as observed from CV and voltage-efficiency test, applied to C-I and C-II was 1.0 V and 1.5 V, respectively. Figure 10, shows the capacitance retention curves for both C-I and C-II, which was around 76 % and 91 %, respectively. On observation, higher capacitance retention was noticed for C-II, when compared with that of C-I. These results, indicates good stability of C-II even at 1.5 V. The lower values of capacitance retention for C-I could have been because of the oxygen evolving reactions from the positive end (Abbas et al. 2015). However, in addition to long term stability, the impedance behavior is also a crucial parameter from which the time lapse for energy deliverance could be affected (Barsoukov & Macdonald, 2005).

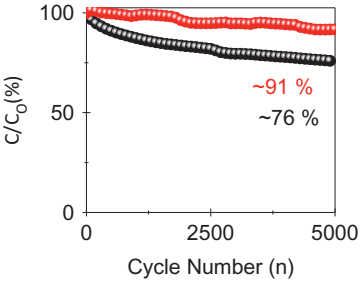

Figure 10: Capacitance retention curves obtained by measuring continuous galvanostatic charge & discharge cycles at a cell current density of 1 A/g (red: C-II, black: C –I). C_0 = refers to values of capacitance at the first cycle. C-I (nickel-stainless steel) and C-II (graphite).

Impedance behaviors were obtained via PEIS technique and were represented by Nyquist plot. Figure 11, shows the Nyquist plot of both C-I and C-II. For both C-I and C-II, the Nyquist plot shows a semi-circle at high frequency range which are related to electron diffusion (also known as charge transfer resistance, CTR) (Barsoukov & Macdonald, 2005). These CTRs are likely to be contributed either by electron diffusion at the pore grain boundaries of the CNF matrix (Pérez et al. 2013) or from redox reactions. The intercept at the real Z' is generally assigned to the equivalent series resistance (ESR), provides an information about the equivalent resistance of a cell which typically includes current collectors, membranes (separators), electrolyte ionic conductivities and active material's resistance (Barsoukov & Macdonald, 2005). The ESR for both C-I and C-II was around 0.18 ohm. cm^2 and 2.9 ohm. cm^2 respectively. The higher ESR for C-II might be related to the conductivity issues of graphite plate which could reduce the maximum power density. Table 2 shows the summary of the electrochemical performances. The possible strategies to reduce the ESR of the device, irrespective of application scale, i. e. either micro or grid based devices, could be via: (1) replacement of better design of current collectors in terms of their electrical contact with the active materials and/or (2) replacement with highly conductive carbon materials as current collectors.

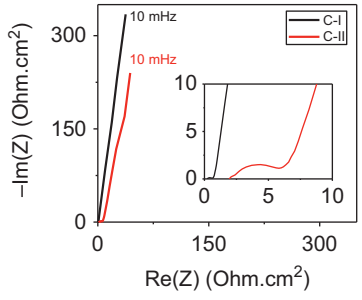

Figure 11: Nyquist plots of C-I and C-II (normalized in terms of geometrical area). C-I (nickel-stainless steel) and C-II (graphite).

Table 2: Summary of the electrochemical performances.

Parameters	C-I	C-II
Mass loading of Fe_2O_3-PCNFs (mg/cm^2)	2.6	2.9
Cell voltage (V)	1.0	1.5
Cell capacitance (F/g)	8.73	16.16
Cell energy density (Wh/kg)	1.21	5.05
Cell power density (W/kg)	445.40	571.07
Capacitance retention (%), 5,000 cycles	76	91
Cell ESR (Ohm. cm^2)	0.18	2.9
Maximum power density* (W/kg)	330	31

Source: *See reference for calculation Gromadskyi et al. (2015).
Note: C-I (nickel-stainless steel) and C-II (graphite). (ESR = equivalent series resistance).

In regards to the first aspect, good electrical contact of electrode material with current collectors, especially in case of self-standing active materials is vital. As mentioned before, the prototype cell was enclosed with metallic aluminum plates and etched graphite plates to ensure good contacts between Fe_2O_3-PCNFs films and graphite plate. However, these tactics could be further improved by using other advanced etching techniques (such as laser engraving). In regards to the second aspect, the graphite could be replaced by other highly

conductive carbon materials such as Carbon nanotubes (CNTs) or graphene papers. Some of the authors like Marco et al. even claims that the conductivity achieved with CNTs could be as equivalent to that of gold current collectors (Notarianni et al. 2014). Graphene papers could be an another promising replacement not only because of their highly conductive property, but also due to ease in production of large geometrical area flexible current collectors which can be easily applicable to micro or grid based devices (Chee et al. 2016).

4 Summary & Conclusions

In conclusions, the perspective in using carbon (graphite) current collectors to enhance the energy density of a symmetric supercapacitior system based in an aqueous alkaline medium,was validated by using several electrochemical studies. Higher value of energy density was witnessed for graphite when compared with that of nickel-stainless steel current collector system. This improvement was accounted because of: (i) widening of cell voltage and (ii) increase of capacitance due to additional charge contributions happening due to widening of cell voltage (redox reactions: $Fe^0/Fe^{2+}/Fe^{3+}$; di-hydrogen production and chemisorption). Lastly, various promising strategies was proposed to improve the resistance related issues of graphite, providing an ease in producing high energy density aqueous micro or macro-supercapacitors.

Acknowledgements: The authors thank Doris Cadavid and Marti Biset for their support during TEM analysis and María Dolores González Candela for BET measurements. IREC also acknowledges additional support by IDIADA AUTOMOTIVE TECHNOLOGY, S.A.

Funding: This work was supported by the European Regional Development Funds (ERDF, FEDER Programa Competitivitat de Catalunya 2007–2013).

References

Abbas, Q., P. Ratajczak, P. Babuchowska, A. L. Comte, D. Belanger, T. Brousse, and F Beguin. 2015. "Strategies to Improve the Performance of Carbon/Carbon Capacitors in Salt Aqueous Electrolytes." *Journal of the Electrochemical Society* 162:A5148–57.

Barsoukov, E., and J. R Macdonald. 2005. *Impedance Spectroscopy: Theory, Experiment, and Applications*. New Jersey, USA: John Wiley & Sons, Inc., Hoboken, New Jersey.

Béguin, F., V. Presser, A. Balducci, and E Frackowiak. 2014. "Carbons and Electrolytes for Advanced Supercapacitors." *Advanced Materials* 26:2219–51.

Binitha, G., M. S. Soumya, A. A. Madhavan, P. Praveen, A. Balakrishnan, K. R. V. Subramanian, and N Sivakumar. 2013. "Electrospun α-Fe_2O_3 Nanostructures for Supercapacitor Applications." *Journal of Materials Chemistry A* 1:11698.

Brousse, T., D. Bélanger, and J. W Long. 2015. "To Be or Not To Be Pseudocapacitive?" *Journal of the Electrochemical Society* 162:A5185–A5189.

Chee, W. K., H. N. Lim, Z. Zainal, N. M. Huang, I. Harrison, and Y Andou. 2016. "Flexible Graphene-Based Supercapacitors: A Review." *Journal of Physics Chemistry C*, 120:4153–72.

Dai, Z., C. Peng, J. H. Chae, K. C. Ng, and G. Z Chen. 2015. "Cell Voltage Versus Electrode Potential Range in Aqueous Supercapacitors." *Scientific Reports* 5:9854.

Demarconnay, L., E. Raymundo-Piñero, and F Béguin. 2010. "A Symmetric Carbon/Carbon Supercapacitor Operating at 1.6 V by Using a Neutral Aqueous Solution." *Electrochemistry Communications* 12:1275–8.

Fic, K., G. Lota, M. Meller, and E Frackowiak. 2012. "Novel Insight Into Neutral Medium as Electrolyte for High-Voltage Supercapacitors." *Energy Environ. Sci* 5:5842–50.

Flox, C., C. Fabrega, T. Andreu, A. Morata, M. Skoumal, J. Rubio-Garciaa, and J. R Morante. 2013. "Highly Electrocatalytic Flexible Nanofiber for Improved Vanadium-Based Redox Flow Battery Cathode Electrodes." *RSC Advances* 3:12056.

Gao, Q., L. Demarconnay, E. R. Pineroa, and F Beguin. 2012. "Exploring the Large Voltage Range of Carbon/Carbon Supercapacitors in Aqueous Lithium Sulfate Electrolyte." *Energy & Environmental Science* 5:9611.

Gao, P. C., W. Y. Tsai, B. Daffos, P. L. Taberna, C. R. Perez, Y., Gogotsi, and F Favier. 2015. "Graphene-Like Carbide Derived Carbon for High-Power Supercapacitors." *Nano Energy* 12:197–206.

Gromadskyi, D. G., J. H. Chae, S. A. Norman, and G. Z Chen. 2015. "Correlation of Energy Storage Performance of Supercapacitor with Iso-Propanol Improved Wettability of Aqueous Electrolyte on Activated Carbon Electrodes of Various Apparent Densities." *Applied Energy* 159. doi:10.1016/j.apenergy.2015.08.108.

Laheäär, A., P. Przygocki, Q. Abbas, and F Béguin. 2015. "Appropriate Methods for Evaluating the Efficiency and Capacitive Behavior of Different Types of Supercapacitors." *Electrochemistry Communications* 60:21–5.

Li, Y., Q. Li, L. Cao, X. Cui, Y. Yang, P. Xiao, and Y Zhang. 2015. "The Impact of Morphologies and Electrolyte Solutions on the Supercapacitive Behavior for Fe_2O_3 and the Charge Storage Mechanism." *Electrochimica Acta* 178:171–8.

Lukatskaya, M. R., B. Dunn, and Y Gogotsi. 2016. "Multidimensional Materials and Device Architectures for Future Hybrid Energy Storage." *Nature Communications* 7:12647.

Ma, Z., X. Huang, S. Dou, J. Wu, and S Wang. 2014. "One-Pot Synthesis of Fe_2O_3 Nanoparticles on Nitrogen-Doped Graphene as Advanced Supercapacitor Electrode Materials." *The Journal of Physical Chemistry C* 118:17231–9.

Notarianni, M., J. Liu, F. Mirri, M. Pasquali, and N Motta. 2014. "Graphene-Based Supercapacitor with Carbon Nanotube Film

as Highly Efficient Current Collector." *Nanotechnology* 25:435405.

Pérez, C. R., S.-H. Yeon, J. Ségalini, V. Presser, P.-L. Taberna, P. Simon, and Y Gogotsi. 2013. "Structure and Electrochemical Performance of Carbide-Derived Carbon Nanopowders." *Advanced Functional Materials* 23:1081–9.

Ratajczak, P., K. Jurewicz, and F Béguin. 2013. "Factors Contributing to Ageing of High Voltage Carbon/Carbon Supercapacitors in Salt Aqueous Electrolyte." doi:10.1007/s10800-013-0644–0.

Ratajczak, P., K. Jurewicz, P. Skowron, Q. Abbas, and F Béguin. 2014. "Effect of Accelerated Ageing on the Performance of High Voltage Carbon/Carbon Electrochemical Capacitors in Salt Aqueous Electrolyte." *Electrochimica Acta* 130:344–50.

Ryu, W.-H., J. Shin, J.-W. Junga, and I.-D Kim. 2013. "Cobalt(Ii) Monoxide Nanoparticles Embedded in Porous Carbon Nanofibers as a Highly Reversible Conversion Reaction Anode for Li-Ion Batteries." *Journal of Materials Chemistry A* 1:3239.

Salanne, M., B. Rotenberg, K. Naoi, K. Kaneko, P. L. Taberna, C. P., Grey, and P Simon. 2016. "Efficient Storage Mechanisms for Building Better Supercapacitors." *Nature Energy* 1:16070.

Simon, P., Y. Gogotsi, and B Dunn. 2014. "Where Do Batteries End and Supercapacitors Begin?" *Science (New York, N.Y)* 343:1210–11.

Stoller, M. D., and R. S Ruoff. n.d. "Best Practice Methods for Determining an Electrode Material's Performance for Ultracapacitors." doi:10.1039/c0ee00074d.

Thommes, M., K. Kaneko, A. V. Neimark, J. P. Olivier, F. Rodriguez-Reinoso, J. Rouquerol, and K. S. W Sing. 2015. "Physisorption of Gases, with Special Reference to the Evaluation of Surface Area and Pore Size Distribution." (IUPAC Technical Report). Pure and Applied Chemistry (Vol. 87).

Wang, D., Y. Li, Q. Wang, and T Wang. 2012. "Nanostructured Fe_2O_3–Graphene Composite as a Novel Electrode Material for Supercapacitors." *Journal of Solid State Electrochemistry* 16:2095–102.

Wu, Y., P. Zhu, M. V Reddy, B. V. R. Chowdari, and S Ramakrishna. 2014. "Maghemite Nanoparticles on Electrospun CNFs Template as Prospective Lithium-Ion Battery Anode." *ACS Applied Materials & Interfaces* 6:1951–8.

Zhang, B., F. Kang, J. M. Tarascon, and J. K Kim. 2015. "Recent Advances in Electrospun Carbon Nanofibers and Their Application in Electrochemical Energy Storage." *Progress in Materials Science* 76:319–80.